

pubs.acs.org/JACS Article

# Deterministic Synthesis of a Two-Dimensional MAPbl<sub>3</sub> Nanosheet and Twisted Structure with Moiré Superlattice

Shuchen Zhang, Ke Ma, Biao Yuan, Jiaqi Yang, Yuan Lu, Dewei Sun, Jee Yung Park, Zitang Wei, Arun Mannodi-Kanakkithodi, Yi Yu, Libai Huang, Timothy J. Pennycook, and Letian Dou\*



Cite This: J. Am. Chem. Soc. 2024, 146, 27861–27870



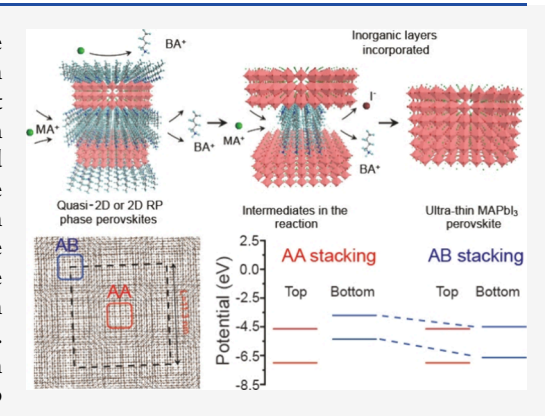
**ACCESS** I

III Metrics & More

Article Recommendations

s Supporting Information

**ABSTRACT:** The synthesis of extremely thin 2D halide perovskites and the exploration of their interlayer interactions have garnered significant attention in current research. A recent advancement we have made involves the development of a successful technique for generating ultrathin MAPbI<sub>3</sub> nanosheets with controlled thickness and an exposed intrinsic surface. This innovative method relies on utilizing the Ruddlesden–Popper (RP) phase perovskite (BA<sub>2</sub>MA<sub>n-1</sub>Pb<sub>n</sub>I<sub>3n+1</sub>) as a template. However, the precise reaction mechanism remains incompletely understood. In this work, we systematically examined the dynamic evolution of the phase conversion process, with a specific focus on the influence of inorganic slab (composed of  $[PbI_6]^{4-}$  octahedrons) numbers on regulating the thickness and quality of the resulting MAPbI<sub>3</sub> nanosheets. Additionally, the atomic structure is directly visualized using the transmission electron microscopy (TEM) method, confirming its exceptional quality. To illustrate interfacial interactions in ultrathin structures, artificial moiré super-



lattices are constructed through a physical transfer approach, revealing multiple localized high-symmetry stacks within a distinctive square moiré pattern. These findings establish a novel framework for investigating the physics of interfacial interactions in ionic semiconducting crystals.

#### 1. INTRODUCTION

Organic—inorganic hybrid halide perovskites with a typical three-dimensional (3D) framework stand out in photovoltaic research due to their remarkable electrical and optical properties, <sup>1–4</sup> including high carrier mobilities, long carrier diffusion lengths, high absorption coefficients, and tunable optical bandgaps. <sup>5–8</sup> Unlike conventional III—V semiconducting materials, one of the most attractive features of perovskites is their easy bandgap engineering, which can be achieved by controlling stoichiometry and/or dimensionality. <sup>9,10</sup> The strong correlation between structures and optical properties enables the rapid development of preparation methods and synthetic conditions for exploring various dimensionalities of perovskites. <sup>11–13</sup>

In recent years, significant advancements have been made in the development of low-dimensional (LD) lead halide perovskites, ranging from zero-dimensional quantum dots and nanoparticles <sup>14,15</sup> to one-dimensional nanowires and nanorods, <sup>16,17</sup> and two-dimensional nanosheets and nanoplates. <sup>18,19</sup> The distinct characteristics resulting from reduced dimensions, such as quantum confinement effects, high photoluminescence quantum yield, and tunable band structures, hold substantial potential for fundamental research in physics and their incorporation into contemporary high-performance light-emitting devices. <sup>20,21</sup> Notably, the attention

has been drawn toward layered two-dimensional (2D) perovskites, composed of nanometer-thick layers of hybrid halide perovskite separated by organic cation-based spacing layers, due to their improved stability and structural adjustability. 22,23 Among all kinds of 2D perovskites, a prominent example is the Ruddlesden-Popper (RP) perovskites with the chemical formula  $L_2A_{n-1}B_nX_{3n+1}$ , where L represents monovalent bulky ligands with alkyl or aromatic components, A denotes a small organic cation, B signifies a metal cation, X stands for a halide, and n indicates the number of inorganic slabs in each layer. Particularly compared with Dion Jacobson (DJ) phase perovskite, the thickness of RP phase perovskites can be precisely regulated through additional mechanical exfoliation, enabling the acquisition of very thin layers such as  $(BA)_2(MA)_{n-1}Pb_nI_{3n+1}$  with *n* ranging from 1 to 4 from the corresponding bulk single crystals.<sup>24</sup> Extensive investigations have been conducted on the light-matter interaction in uniform 2D perovskite crystals, yielding significant advance-

Received: July 28, 2024
Revised: August 17, 2024
Accepted: September 19, 2024
Published: September 27, 2024





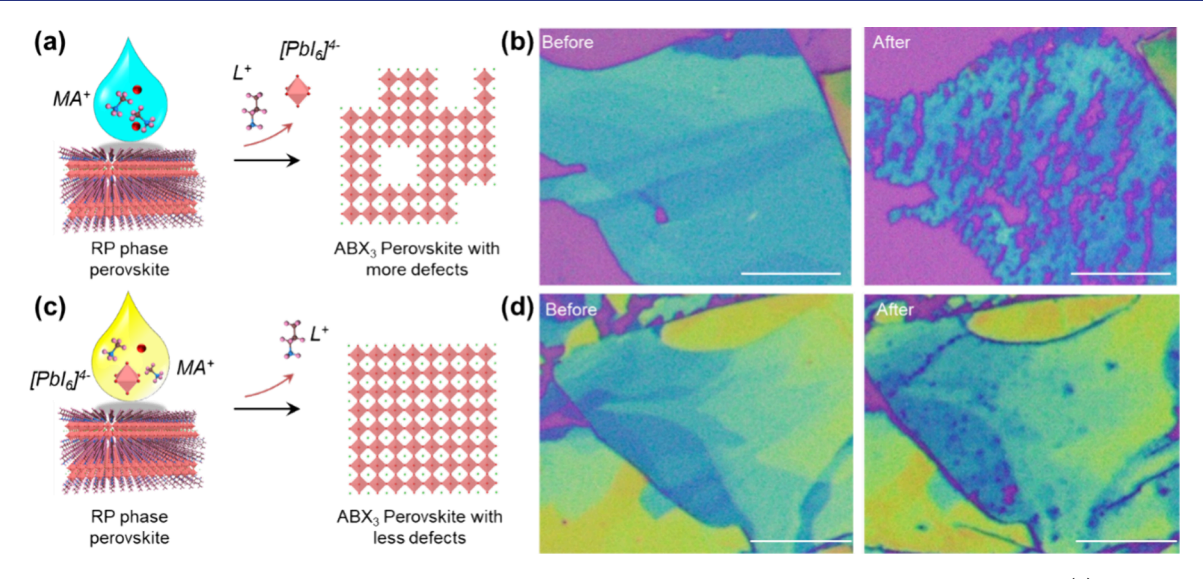


Figure 1. Designed IPA equilibrium solution strategy to realize MAPbI<sub>3</sub> perovskite using 2D RP perovskite as a template. (a) Schematic to show the reaction result by using IPA solution only containing MAI, indicating significant dissolution of perovskites and more defects. (b) Comparison between before (left) and after (right) reaction after 3 min in only MAI IPA solution indicates dissolution of RP phase perovskites. Scale bars are 10 μm. (c) Schematic to show the reaction result by using MAI/PbI<sub>2</sub> equilibrium solution, indicating the well-preserved structure of perovskite. (d) Comparison between before (left) and after (right) reaction after 15 min in MAI/PbI, equilibrium solution indicates less dissolution of RP phase perovskites and good preservation of shape. Scale bars are both 10  $\mu$ m.

ments.<sup>25</sup> Nevertheless, a comprehensive understanding of the photophysical characteristics at the interface of 2D perovskite vertical junctions is hindered by the absence of direct interfacial electron coupling, which is impeded by the presence of bulky organic ligands.<sup>26</sup>

Hence, to build the effective heterostructure, there is a requirement to produce extremely thin LD perovskite materials with an exposed intrinsic inorganic surface, a task that is challenging due to the fragile and ionic nature of the structure. By utilizing methylammonium iodide (MAI) or formamidinium iodide (FAI) vapor, lead iodide (PbI2) nanoplates deposited on substrates have been successfully transformed into MAPbI<sub>3</sub>/FAPbI<sub>3</sub> perovskites with high crystalline quality, enabling thickness variations from a few to hundreds of nanometers.<sup>27–30</sup> However, enhancing the crystal quality of perovskites remains imperative, primarily owing to the elevated temperature necessary for the conversion process. Additionally, the operability within heterostructure fabrication is further hindered by the influence of polar solvents involved in the transfer process. Our recent studies have indicated that 2D RP phase perovskites can act as templates for producing ultrathin MAPbI<sub>3</sub> nanosheets, which can serve as fundamental components for creating vertical junctions.<sup>31</sup> Nevertheless, the exact conversion mechanism remains incompletely understood. Herein, this research would systematically investigate the dynamic conversion process in the reaction solution, including the transition from the 2D RP phase to the 3D phase, explaining the substitution of small cations (MA+) with bulky ligands (L<sup>+</sup>), and the fusion of adjacent inorganic layers. Notably, the thickness of the resulting MAPbI<sub>3</sub> can be controlled by either the thickness (or layer numbers) or the nanometer values of RP phase perovskites. It was observed that enhancing the n values of 2D perovskites can improve the crystal quality of ultrathin MAPbI<sub>3</sub>, with the high quality being validated through atomic imaging of inorganic layers and organic cations. In addition, by successfully synthesizing ultrathin MAPbI<sub>3</sub> perovskite on diverse substrates, an artificial

twisted MAPbI3 moiré superlattice was constructed to showcase a vertical junction. High-resolution transmission electron microscopy (HRTEM) distinctly exhibited squared moiré patterns with localized high-symmetry stacking. Through integration with first-principles calculations, it was disclosed that local interlayer coupling can be intensified through moiré potential modulation, resulting in distinctive properties that exhibit promise for future research pursuits.

#### 2. RESULTS AND DISCUSSION

2.1. Equilibrium Solution Design to Realize Ultrathin MAPbl<sub>3</sub> Perovskite Nanosheets. To create MAPbl<sub>3</sub> perovskite microplates/film, a standard procedure involves utilizing a solution of dissolved MAI in isopropyl alcohol (IPA) to interact with a solid-state PbI<sub>2</sub> film. <sup>32,33</sup> Given the limited solubility of PbI2 in IPA, this synthesis reaction for perovskites is categorized as a solid-liquid reaction, resulting in the formation of a minor quantity of octahedral  $[PbI_6]^{4-}$  in the solution at equilibrium (Figure S1). Upon reaching equilibrium (Formula 1), the concentration of [PbI<sub>6</sub>]<sup>4-</sup> can be approximated by  $c([PbI_6]^{4-})=K_1c(I^-)^4$ , where  $K_1$  represents the equilibrium constant of the reaction and is of a notably low value. Obviously, the concentration of [PbI<sub>6</sub>]<sup>4-</sup> is significantly influenced by the iodide anion concentration (or MAI concentration). Subsequently, if this "equilibrium solution" comprising MA<sup>+</sup>, I<sup>-</sup>, and [PbI<sub>6</sub>]<sup>4-</sup> is employed to process a thin RP phase perovskite crystal, according to our previous results,<sup>31</sup> it will directly transform the RP perovskite (2D phase) into a MAPbI<sub>3</sub> perovskite (3D phase) by eliminating the ligand cation (L+) and releasing excess I- from the RP perovskite crystal matrix (Formula 2). It is evident that while MA<sup>+</sup> is advantageous, I<sup>-</sup> is not conducive to this conversion reaction. Hence, it is postulated that by converting I- into [PbI<sub>6</sub>]<sup>4-</sup>, the equilibrium solution contains a higher proportion of MA+ compared to I-, thereby rendering it favorable for the reaction exhibited in Formula 2. Furthermore, if the in situ formation of the MAPbI<sub>3</sub> perovskite sheet with a 3D phase is

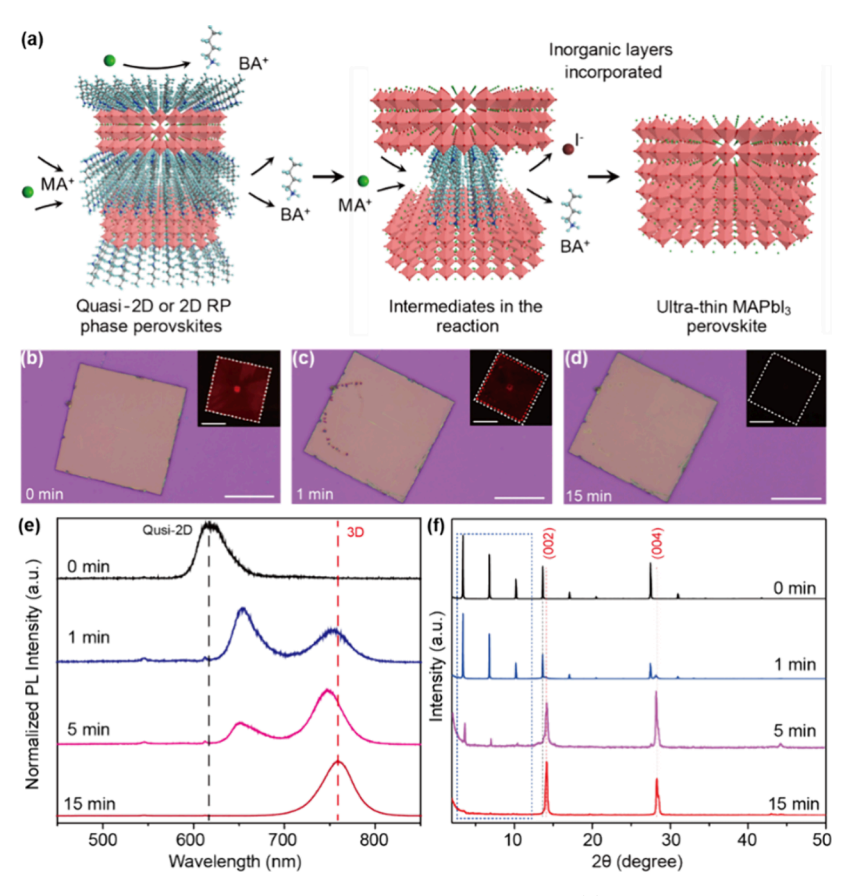


Figure 2. Conversion mechanism based on the MAI/PbI<sub>2</sub> equilibrium solution method. (a) A proposed mechanism to represent the releasing of bulky ligands and insert of MA<sup>+</sup> cations to form MAPbI<sub>3</sub> perovskite structure. (b–d) A quasi-2D RP phase perovskite nanocrystal, (BA)<sub>2</sub>MA<sub>2</sub>Pb<sub>3</sub>I<sub>10</sub>, was used to prove the conversion mechanism by tracking the reaction with the time, 0 min (b), 1 min (c), and 15 min (d). The insets are the corresponding PL emission images with the UV—vis detector. All the scale bars are 20  $\mu$ m. (e) Corresponding PL emission spectra of the perovskite nanocrystal with different reaction times. The small blueshift for increasing the reaction time from 1 to 5 min may originate from the diffusion of more MA<sup>+</sup> cations into lattice to eliminate lattice defects. (f) XRD characterizations of the perovskites on silicon substrate with different reaction times. The signals marked by rectangles with dashed lines represent the quasi-2D RP phase perovskite, and the red dashed lines represent MAPbI<sub>3</sub> perovskite with a 3D structure.

exceedingly thin, it will be susceptible to dissolution with the assistance of I to generate [PbI<sub>6</sub>]<sup>4-</sup> (Formula 3). Building upon this analysis, it is further conjectured that the presence of [PbI<sub>6</sub>]<sup>4-</sup> in the equilibrium solution may aid in impeding the dissolution of MAPbI3, consequently resulting in the production of superior quality thin MAPbI<sub>3</sub> crystals. To illustrate this phenomenon, two types of IPA solutions, one containing solely MAI and the other equilibrated by MAI/PbI<sub>2</sub> with the proper ratio, were employed to treat RP phase halide perovskites, as depicted in Figure 1a. It was evident that significant dissolution of RP phase perovskite occurred in the pure-MAI solution after 3 min (Figure 1a,b), whereas the perovskite shape remained intact in the MAI/PbI<sub>2</sub> equilibrium solution even after 15 min (Figure 1c,d). Through complementary photoluminescence (PL) emission analysis (Figure S2), it was observed that the distinctive characteristics of RP phase perovskite vanished following treatment with the equilibrium solution, with the emergence of emission traits specific to MAPbI<sub>3</sub> perovskites. This suggests the complete substitution of bulky ligands with MA+ cations within the lattice, which is in agreement with the aforementioned assumption. Consequently, a viable strategy for producing ultrathin MAPbI<sub>3</sub> perovskites through equilibrium solution conversion is reasonably proposed, utilizing 2D or quasi-2D RP phase perovskites as a template.

$$PbI_{2}(s) + 4I^{-} \rightleftharpoons [PbI_{6}]^{4-}K_{1} = c(PbI_{6}^{4-})/c(I^{-})^{4}$$
 (1)

$$L_{2}MA_{n-1}Pb_{n}I_{3n+1}(s) + MA^{+}$$

$$\Rightarrow nMAPbI_{3}(s) + 2L^{+} + I^{-}K_{2}$$

$$= c(L^{+})^{2}c(I^{-})/c(MA^{+})$$
(2)

$$MAPbI_3(s) + 3I^- \rightleftharpoons MA^+ + [PbI_6]^{4-}K_3$$
  
=  $c(MA^+)c(PbI_6^{4-})/c(I^-)^3$  (3)

**2.2.** Dynamic Conversion Mechanism from 2D Perovskite to 3D Perovskite. To gain a deeper comprehension of the conversion process, a potential dynamic conversion mechanism is further proposed, as depicted in Figure 2a. Once treated with the equilibrium solution, the conversion process involves the initial release of bulky ligands located on the upper surface and in close proximity to the edge of RP phase perovskites due to concentration-induced diffusion. This release of bulky ligands leads to the formation of interlayer channels between the inorganic layers composed of [PbI<sub>6</sub>]<sup>4-</sup> octahedrons, facilitating the smooth diffusion of MA<sup>+</sup> cations to replenish the vacancies within the lattice. Subsequently, as the bulky ligands are substituted by MA<sup>+</sup> cations, the inorganic framework with an unaltered surface is exposed, showcasing

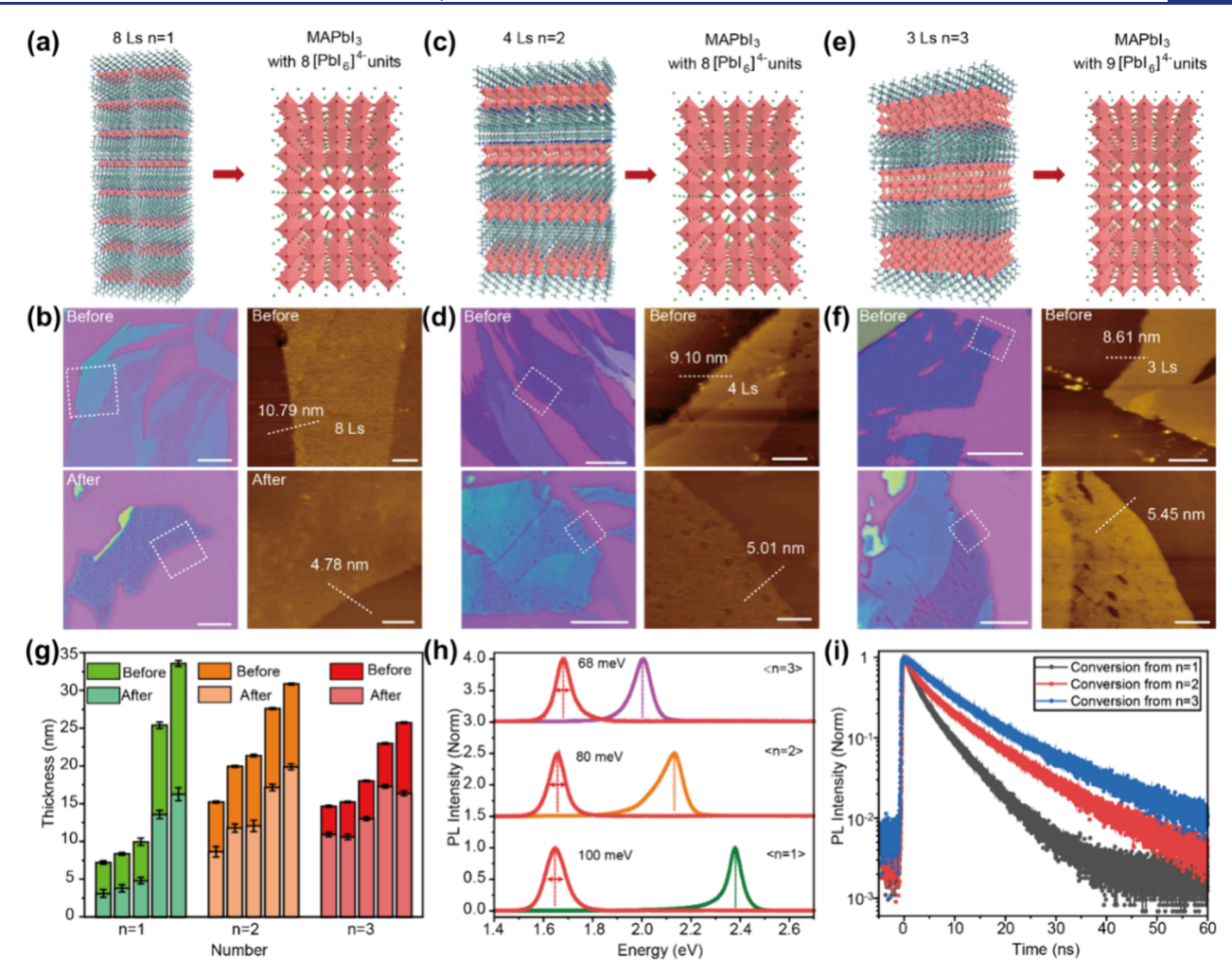


**Figure 3.** Thickness controlling by different 2D and quasi-2D RP phase perovskites. (a, b) Eight layers (8 Ls) 2D RP phase perovskites (n = 1) for conversion to MAPbI<sub>3</sub> perovskites. (c, d) Four layers (4 Ls) quasi-2D perovskites (n = 2) for conversion to MAPbI<sub>3</sub> perovskites. (e, f) Three layers (3 Ls) quasi-2D RP phase perovskites (n = 3) for conversion to MAPbI<sub>3</sub> perovskites. All the scale bars for optical images are 20  $\mu$ m and for AFM images are 2  $\mu$ m. (g) Thickness changes before and after conversion by using different RP phase perovskites with n = 1, 2, and 3. (h) Comparison on the PL emission spectra of MAPbI<sub>3</sub> perovskites with a similar thickness ( $\sim$ 5 nm) converted from different RP phase perovskites with n = 1, 2, and 3. (i) Comparison on the corresponding PL lifetime of MAPbI<sub>3</sub> perovskites in panel (h).

the lattice structure as the thinned-MAPbI $_3$ . Moreover, owing to the short distance between the interlayers, the adjacent inorganic layers bond together by sharing an iodide ion (I $^-$ ) between two [PbI $_6$ ] $^{4-}$  octahedra and eliminating excess iodide ions. Upon completion of bonding between the layers, a MAPbI $_3$  structure with an increased thickness is formed. The final thickness of synthesized MAPbI $_3$  is solely dictated by the quantity of inorganic layers present in the original RP phase perovskite sample. Furthermore, without causing harm to the inorganic frameworks throughout the entire conversion process, the synthesized MAPbI $_3$  also mirrors the same morphology as that of the original RP phase perovskite.

To rigorously assess the proposed dynamic mechanism, a quasi-2D RP phase perovskite nanocrystal,  $(BA)_2MA_2Pb_3I_{10}$ , was synthesized utilizing the solution—air interface method<sup>34</sup> and subsequently transferred onto a  $SiO_2$  (300 nm)/Si substrate to monitor its temporal evolution (Figure 2b–d). The initial state of the sample, as shown in Figure 2b, exhibited a uniform red emission, as evidenced by the corresponding photoluminescence (PL) spectra with an emission wavelength of approximately 610 nm (Figure 2e), characteristic of quasi-2D RP phase perovskite with n=3. Upon treatment with the

equilibrium solution, a noticeable darkening of the emitting color, particularly pronounced at the edges, was observed (Figure 2c). Analysis of the PL spectra (Figure 2e) revealed a remarkable phenomenon where two new emission peaks, situated at approximately 650 and 740 nm, replaced the original emission peak (~610 nm) from the quasi-2D RP phase perovskite. Subsequent detailed characterizations conducted at various positions on the sample (Figure S3) elucidated that the emission peak at ~650 nm predominantly emanated from the central portion of the perovskite crystal, while the emission at ~740 nm originated from the edge. The former emission can be attributed to the reduction of lattice distortion in the quasi-2D RP phase perovskite structure due to the replacement of bulky ligands (BA+), despite the unchanged number of inorganic layers, a phenomenon not previously reported.<sup>35</sup> The latter emission arises from the incorporation of two adjacent inorganic frameworks devoid of ligands at the edge, leading to their convergence into a thicker 3D structure. This emission could be further enhanced by incorporating more inorganic frameworks with an increased reaction time.

As the reaction progressed, the original red emission color with a shorter wavelength completely disappeared, as

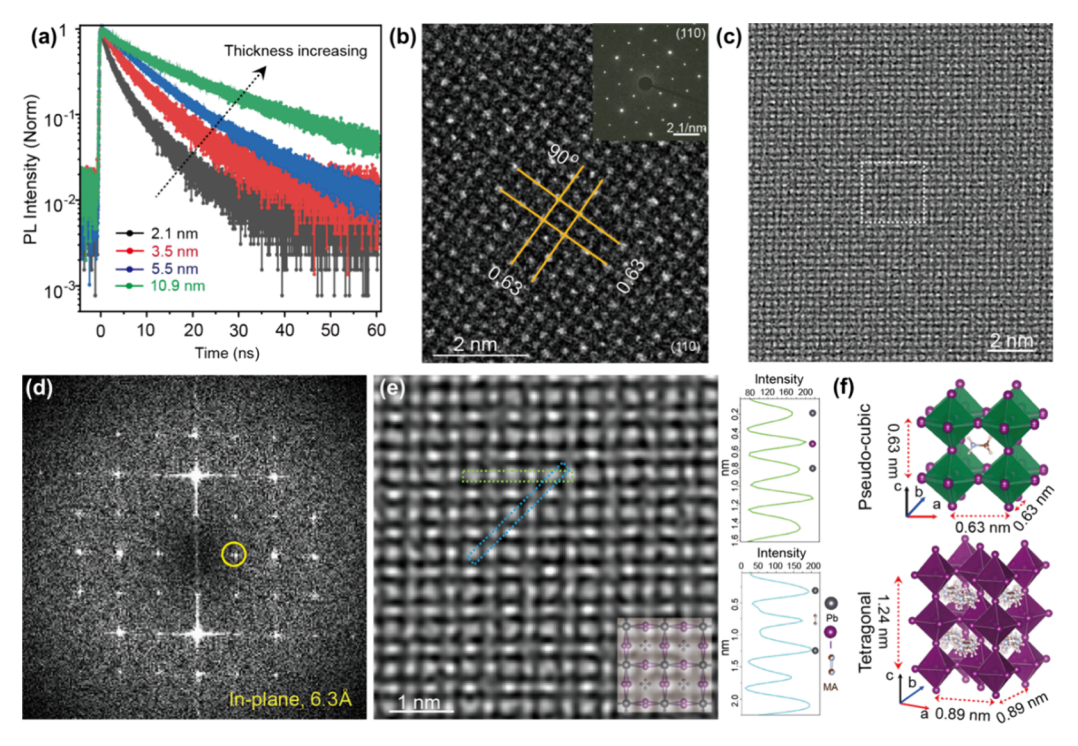


Figure 4. Effect of thickness on lifetime and TEM characterization. (a) PL lifetime of MAPbI<sub>3</sub> perovskite with different thickness, varying from about 2-10 nm. (b) HRTEM image of the obtained MAPbI<sub>3</sub> perovskite with the thickness of about 5 nm. Corresponding SEAD pattern of MAPbI<sub>3</sub> perovskite. (c) Raw phase image retrieved by the single sideband (SSB) ptychographic method. (d) Corresponding Fourier transform of the phase image in panel (c). Yellow circles indicate that the in-plane lattice distance is 6.3 Å. (e) Corresponding enlarged and Wiener filtered image (left) and line profiles along (110) (green) and (200) (blue) directions (right). The inset shows a overlaid structure model indicating the atomic positions. (f) The pseudocubic (Space group Pm3m, a = 6.3 Å) and tetragonal (Space group I4/mcm, a = 8.9 Å, c = 12.4 Å) structures of MAPbI<sub>3</sub> perovskites with different thicknesses and illustrated by HRTEM data (b–d) and XRD results in Figure S9.

evidenced by the PL image in Figure 2d, indicating the completion of the conversion from quasi-2D perovskite to a 3D structure within 15 min. At this juncture, only one peak, located at approximately 755 nm, was discernible in the PL spectrum, exhibiting a smaller redshift (~15 nm) compared to the peak (~740 nm) observed in the early stages of the reaction (Figure 2e). This shift is attributed to the further increase in thickness resulting from the incorporation of all of the inorganic lead iodide layers in the 2D perovskite. This evolution was supported by the X-ray diffraction (XRD) results shown in Figure 2f, and specifically, the XRD signals exclusively exhibited the characteristic peaks originating from quasi-2D perovskite (n = 3) precursors at the initial reaction stage, consistent with reported findings.<sup>24</sup> As the reaction progressed, a discernible trend emerged wherein the peaks of quasi-2D RP phase perovskites, particularly those at small angles, gradually diminished, ultimately yielding two characteristic peaks at  $2\theta = 14.15$  and  $28.40^{\circ}$ . These peaks are ascribed to the orderly vertical stacking of octahedral [PbI<sub>6</sub>]<sup>4-</sup>, confirming the formation of a 3D structure in the final converted products. Collectively, all results furnish unequivocal evidence of the successful conversion of 2D or quasi-2D perovskites to MAPbI<sub>3</sub> with a 3D structure.

**2.3. Thickness Controlling Strategy and Structure Properties.** It is noteworthy that all the 2D RP phase perovskites with varying n values (n = 1, 2, and 3) can serve as templates for achieving the MAPbI<sub>3</sub> perovskite structure using the equilibrium solution conversion method. This presents a viable approach for regulating the thickness of MAPbI<sub>3</sub> by adjusting the nanometer values and layer numbers of RP phase perovskites. For instance, as illustrated in Figure 3a-f, MAPbI<sub>3</sub>

perovskites with a comparable thickness of approximately 5 nm, as determined by atomic force microscopy (AFM), were successfully obtained utilizing RP phase perovskites with n = 1(8 layers), n = 2 (4 layers), and n = 3 (3 layers), respectively. Notably, the most significant variation in thickness between pre- and postconversion was observed in the RP phase perovskites with n = 1, likely attributed to the presence of bulky ligands within the lattice of RP phase perovskites, particularly pronounced in n = 1 perovskite. Intriguingly, further analysis (Figure 3g) of the thickness alterations of RP phase perovskites pre- and postconversion suggests a consistent ratio for different perovskite samples with the same RP phase, namely, 57% for n = 1, 41% for n = 2, and 29% for n = 3. These consistent ratios closely align with the occupancy of bulky ligands in the respective original RP phase perovskites with different n values (refer to Table S1), indicating no loss of the inorganic layers during the conversion process. Moreover, additional assessments of steady-state PL in Figure 3h also confirm the successful conversion, albeit revealing slight discrepancies in the emission peak positions, ranging from 755 nm for n = 1-745 nm for n = 3. Given the diminished confinement effect with increased thickness, the minor variation in thickness between the two samples acquired from RP perovskites with different n values is not the primary cause of this discrepancy in emission peak. Instead, defects are commonly considered to be the pivotal factor influencing the optical characteristics of perovskites by trapping excitons/ carriers. Hence, this discrepancy can be attributed to the structural defect, including vacancy, interfacial merging, and lattice stretching. Furthermore, the broadened full width at

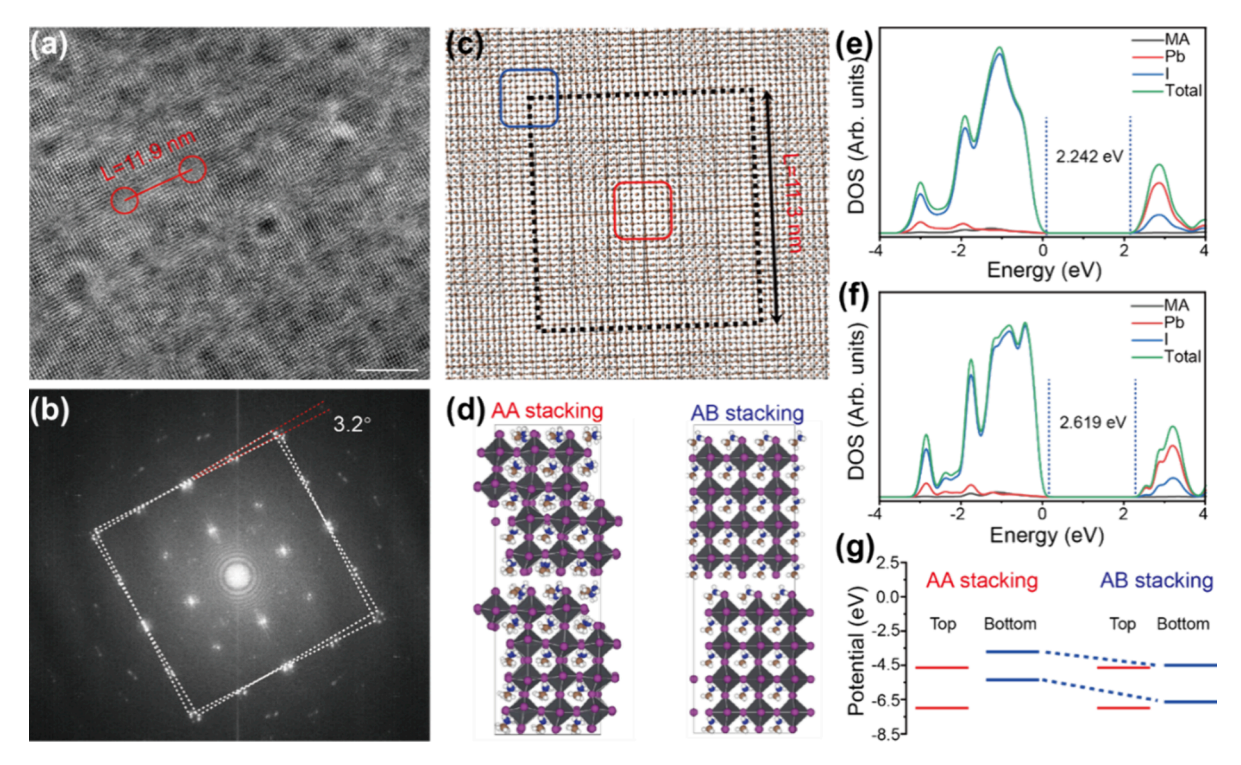


Figure 5. Moiré superlattice formed by twisted bilayers of MAPbI<sub>3</sub> perovskite nanosheets. (a) Moiré pattern and its periodicity of twisted bilayers of MAPbI<sub>3</sub> perovskite nanosheets indicated by the HRTEM. The scale bar is 10 nm. (b) Selected area electron diffraction measurements for the region of panel (a). Two sets of diffraction spots and a formed intersection angle of  $3.2^{\circ}$  indicate that bilayer MAPbI<sub>3</sub> nanosheets are twisted by  $3.2^{\circ}$ . (c) Perpendicular view of the simulated bilayer MAPbI<sub>3</sub> nanosheets with the twist angle of  $3.2^{\circ}$ , forming a moiré superlattice with periodicity L = 11.3 nm. To clearly demonstrate the moiré pattern, a simplified and squared lattice was used. (d) Two distinct localized stacking structures observed in panel (c), AA-stacking (left) and AB-stacking (right). (e, f) Calculated density of states for AA-stacking (e) and AB-stacking obtained by first-principles calculations.

half-maximum (fwhm) of the peak at the 755 nm wavelength also supports this explanation.

The analysis presented above suggests that the MAPbI<sub>3</sub> sample containing n = 1 RP phase perovskite exhibits more defect species, as illustrated in Figure 3h. It is indicated that the defect species of the as-synthesized MAPbI<sub>3</sub> perovskites could be reduced by increasing the *n* values of RP phase perovskites. To support this interpretation, the charge carrier dynamics of three distinct MAPbI<sub>3</sub> perovskites of similar thickness were compared by analyzing time-resolved PL (TRPL) spectra at the primary steady-state PL peak (~755 nm), which reflects the defect density. The results depicted in Figure 3i reveal a correlation between the PL lifetimes of the final MAPbI<sub>3</sub> perovskites and the n values of the corresponding RP phase perovskite precursors, with larger n values leading to longer lifetimes when excited by a 447 nm laser under a power of 50 nW. Typically, the presence of certain defects offers an additional pathway for exciton recombination, resulting in shorter lifetimes. Therefore, the observed trend of carrier lifetime variations with changes in n values aligns with the aforementioned interpretation. To gain a deeper understanding of the impact of n values on the defect density of the synthesized MAPbI<sub>3</sub> perovskites, schematics presented in Figure 3a,c,e are utilized to compare the conversion process. During this process, it is necessary to employ more layers of RP phase perovskites with lower n values, such as n = 1, to achieve the same thickness, thereby increasing the number of interfaces involved. This scenario enhances the likelihood of introducing defect species and density during the removal of

ligands in the perovskite matrix, particularly I-vacancies and imperfect interfacial merging. Conversely, high-quality MAPbI<sub>3</sub> perovskite is obtained by utilizing 2D perovskites with higher n values, as they involve fewer interface mergers and exhibit intrinsic stacking closer to that of MAPbI<sub>3</sub> perovskites. Similarly, decreasing the bulky BA<sup>+</sup> cation concentration has the same function as increasing the n value of RP phase perovskites to improve the defect density of the as-synthesized MAPbI<sub>3</sub> nanosheets.

Meanwhile, the PL lifetimes depicted in Figure 4a exhibit a gradual prolongation with increasing thickness, consistent with findings in the literature.<sup>36</sup> The intricate structure of the resulting ultrathin MAPbI<sub>3</sub> perovskite nanosheets was further scrutinized using transmission electron microscopy (TEM). Employing a physical transfer system in conjunction with optical microscopy, the ultrathin MAPbI3 perovskite nanosheets, synthesized directly on polydimethylsiloxane (PDMS), were transferred onto SiNx TEM grids with a thickness of approximately ~5 nm. It is well-known that hybrid perovskites are prone to rapid degradation under electron-beam irradiation, posing significant challenges for TEM characterization, particularly with the synthesized ultrathin sample thickness ranging between 1.2 and 2.4 nm, consisting of only 2to-4 [PbI<sub>6</sub>]<sup>4-</sup> octahedron layers. To mitigate the beam damage issue, a low electron dose, specifically 15 e-Å-2 (e- denoting electrons), was adopted for acquiring high-resolution TEM (HRTEM) images and selected area electron diffraction (SAED) patterns. As depicted in Figure 4b, the HRTEM image displays equal lattice parameters (a and b) in the plane,

both measuring 0.63 nm.<sup>37</sup> The 4-fold in-plane symmetry was corroborated by the SAED patterns, with the absence of diffuse scattering points indicating a single crystal nature of high quality.

To elucidate the atomic arrangement of the ultrathin MAPbI<sub>3</sub> perovskite further, 4D scanning transmission electron microscopy (4D-STEM) was employed. However, in the conventional high-angle annular dark field (HAADF) STEM, sensitive to atomic number distributions, the signal of MA+ is always absent due to the weak scattering of light carbon and nitrogen atoms by the electron beam, resulting solely in the observation of heavy atoms, lead (Pb) and iodine(I), within a tetragonal perovskite structure (Figure S8). In contrast, the ptychographic single sideband (SSB) method, being doseefficient and easily interpretable, facilitated the phase retrieval of both light and heavy atoms in MAPbI3, enabling simultaneous imaging with an annular detector.<sup>38</sup> As exhibited in Figure 4c, all atomic columns are discernible in the phase image, including the lightest MA<sup>+</sup> molecules. The corresponding Fourier transform image (Figure 4d) indicates a higher resolution than the HAADF image (Figure S8), revealing a clear Pb-I-Pb lattice with an interplanar spacing of 6.3 Å, consistent with HRTEM results (Figure 4b), owing to the high dose efficiency of the SSB method that utilizes more electrons for imaging than HAADF STEM. Moreover, the positions of MA+ cations, I and Pb atoms are clearly distinguishable in the profile of the atomic columns (Figure 4e), identified by their distinct peaks. Particularly, the denoised phase image presented in Figure 4e provides further insight into the intact structure of the ultrathin MAPbI<sub>3</sub> nanosheet, revealing elliptical contrasts of iodine columns, suggesting a tilt angle between the upper and lower layers of [PbI<sub>4</sub>] octahedrons. Additionally, the lack of a fixed shape of MA+ molecules may be attributed to the random orientations of rotated MA+ cations within the cubic cage formed by Pb2+ at room temperature. To comprehend the crystal stacking structure better, parameter c, involving the out-of-plane stacking spacing, was extracted from the XRD results. An intriguing observation is the dependence of XRD results on sample thickness, resulting in two distinct sets of diffraction peaks (Figure S9). For thin samples (thickness <20 nm), the diffraction peak occurs at  $2\theta = 14.00^{\circ}$ , while for thick samples (thickness >20 nm), it shifts to  $2\theta = 14.15^{\circ}$ . With Bragg's Law  $(d = \lambda/2\sin\theta)$ , the distances of adjacent faces were calculated as 0.63 nm for thin samples and approximately 0.62 nm for thick samples. It can be inferred that the thin sample exhibits a pseudocubic phase (Space group Pm3m) with parameters a = b = c = 0.63nm (Figure 4d), while the thick sample belongs to a tetragonal phase (Space group I4/mcm, a = 8.9 Å, c = 12.4 Å) as illustrated in Figure 4e. The peaks near 14° are attributed to (001) for the pseudocubic phase and (002) for the tetragonal phase, respectively. This discrepancy may originate from substrate-induced strain, which would significantly affect the vertical stacking spacing for ultrathin MAPbI<sub>3</sub>.

**2.4.** Artificial Twisted MAPbl<sub>3</sub> Moiré Superlattice and Localized Properties. To illustrate homojunctions within thin MAPbl<sub>3</sub> perovskite nanosheets, an artificial twisted superlattice was created by using a physical transfer process. In this process, ultrathin MAPbl<sub>3</sub> nanosheets, each with a thickness of less than 5 nm, were meticulously stacked layer-by-layer along the c-axis direction. Subsequently, the twisted superlattice was observed by using high-resolution transmission electron microscopy (HRTEM), as depicted in Figure

5a. In contrast to the single sheet of as-synthesized ultrathin MAPbI<sub>3</sub> in Figure 4b, the twisted superlattice exhibits distinct squared moiré patterns with a period length (L) of 11.9 nm. Additionally, the corresponding selected area electron diffraction (SAED) pattern of the moiré superlattice in Figure 5b clearly reveals two sets of diffraction spots with an intersection angle of approximately 3.2°, indicating a twist between adjacent sheets of this magnitude. This phenomenon resembles the formation of moiré superlattices observed in twisted graphene or transition-metal dichalcogenides (TMDCs) bilayers.<sup>39,40</sup> Furthermore, a simulated image in Figure 5c was generated using a simplified lattice to represent the top and bottom layers, respectively, accurately replicating the moiré patterns observed in Figure 5a. Moreover, in the context of vertical homojunctions, the precise period (L) of such moiré superlattices is determined by the equation  $L = a_0/$  $\sin \theta$ , where  $a_0$  represents the distance (0.63 nm) of the inplane Bravais lattice and  $\theta$  denotes the twist angle. Consequently, the theoretically calculated period (L) is 11.3 nm (Figure 5c), with a<sub>0</sub> being 6.3 Å for ultrathin MAPbI<sub>3</sub>, directly obtained from the TEM image in Figure 4b. This value aligns well with the measurement in Figure 5a, despite the stacked ultrathin MAPbI<sub>3</sub> perovskite nanosheet not being an atomic monolayer.

Additionally, the simulated image in Figure 5c reveals the presence of at least two distinct types of localized orderly stacking patterns, hereafter referred to as AA-stacking and ABstacking (corresponding to AA and HH stacking, respectively, in ref 40, which presents a similar square lattice), as depicted in Figure 5d, within the moiré structures at the atomic scale. These patterns have been anticipated in a prior literature,<sup>42</sup> with AB-stacking typically demonstrating greater energetic stability owing to potential interlayer H bonds, while AAstacking tends to be less stable. Consequently, unconventional properties may manifest and be delineated through moiré potential. Utilizing the models in Figure 5d, we used density functional theory (DFT) computations to determine the electronic density of states (DOS) for the two localized stacks and extracted their corresponding band gaps as illustrated in Figure 5e,f. In comparison with bulk MAPbI<sub>3</sub> perovskite (Figures S10 and S11), both localized stacking structures exhibit an augmentation in the band gap. However, the augmentation is more pronounced in AB-stacking due to the substantial reconstruction induced by interlayer H bonds. The notable dependence of the band gap on the localized position could result in a spatial modulation of the electronic structure and associated properties. We further computed the relative electronic band edges of the top and bottom layers using an electrostatic potential alignment method. As depicted in Figure 5g, a type-II band alignment would potentially emerge in AAstacking, likely due to interface distortion with repulsion from I-I contact, thereby yielding the possibility of interlayer excitons. Meanwhile, the formation of hybridized excitons in AB-stacking arises from its pseudotype-II band alignment. This suggests that the excitonic properties of perovskite vertical junctions can be manipulated by the twist angles and the coexistence of various local stacking configurations, akin to those of other 2D materials.

# 3. CONCLUSIONS

In summary, we provide reasonable explanation of how we achieve an equilibrium solution to produce ultrathin MAPbI<sub>3</sub> perovskite nanosheets with precise thickness control and

exposed intrinsic surfaces. This is accomplished by utilizing a 2D RP phase perovskite as a template. Based on the analysis of species under reaction equilibrium, the critical aspect enabling this successful transformation involves establishing a reaction environment containing a minimal quantity of octahedral [PbI<sub>6</sub>]<sup>4-</sup>, which hinders the dissolution of the inorganic frameworks of perovskites. Furthermore, the thickness of  $MAPbI_3$  can be effectively regulated by adjusting the n values or inorganic layer numbers within the 2D RP phase perovskite template. Moreover, an increase in the n value also aids in reducing the defect density of the synthesized ultrathin MAPbI<sub>3</sub> perovskite by minimizing the interfacial merging of inorganic frameworks. As an illustration, we constructed an artificial moiré superlattice with a twist angle of 3.2° using the high-quality ultrathin MAPbI<sub>3</sub> perovskite. The resulting moiré pattern displays various localized stacking structures with notable symmetry. Through complementary first-principles calculations, it is revealed that the local interlayer coupling can be strengthened through moiré potential modulation, leading to distinctive properties that warrant further exploration. Our discoveries introduce a novel approach for fabricating ligandfree ultrathin perovskite nanosheets and establish a foundation for investigating photophysics related to interfacial coupling in emerging low-dimensional material systems.

# 4. EXPERIMENTAL SECTION

- 4.1. Chemicals and Materials. Solvents, including anhydrous chlorobenzene (CB), isopropyl alcohol (IPA), hydroiodic acid (HI, 57 wt % in H<sub>2</sub>O), hypophosphorous acid (H<sub>3</sub>PO<sub>2</sub>, 50 wt % in H<sub>2</sub>O), and solid chemicals including PbO powders and lead iodide (PbI<sub>2</sub>) were purchased from Sigma-Aldrich. n-Butylammonium iodide (BA-HI) and methylammonium iodide (MAI) were purchased from Greatcell Solar Ltd. All chemicals were used as received.
- 4.2. Synthesis of 2D and Quasi-2D Perovskite Single Crystals. For the BA<sub>2</sub>PbI<sub>4</sub> crystal, PbO (0.57 mmol) and BAI (0.57 mmol) precursors were used. For BA2MAPb2I7 crystal, PbO (0.59 mmol), BAI (0.43 mmol), and MAI (0.31 mmol) precursors were used. For  $BA_2MA_2Pb_3I_{10}$  crystal, PbO (0.59 mmol), BAI (0.19 mmol), and MAI (0.4 mmol) precursors were used. To grow each crystal, all the precursors were dissolved into an acid mixture containing 0.9 mL of HBr or HI and 0.1 mL of H<sub>3</sub>PO<sub>2</sub> in a 10 mL glass vial and heated to 120 °C in an oil bath [ref S1, Supporting Information]. Once the precursors were completely dissolved, the stirring was terminated and the solution was cooled to room temperature with a cooling rate of 10 deg/10 min. The crystals were collected by vacuum filtration.
- 4.3. Conversion from 2D Perovskites to MAPbl<sub>3</sub> Perovskite Using the Equilibrium Solution Method. The equilibrium solution was made by PbI<sub>2</sub> (10 mg)/MAI (10 mg) in 1 mL of IPA solution. To reach equilibrium, the solution was heated at 40 °C on a hot plate for overnight. Then, 250  $\mu$ L of supernatant of equilibrium solution was used for conversion at room temperature, and reaction times were 1, 5, and 7 min to acquire thin MAPbI<sub>3</sub> perovskites from exfoliated BA2PbI4, BA2MAPb2I7, and BA2MA2Pb3I10 precursors on the silicon substrate, respectively. The reaction was performed in a 4 mL glass vial. After reaction, the samples were washed by 1 mL of CB and IPA mixed solution with the volume ration of 100/3 and further annealed at 55-58 °C for 10 min.
- 4.4. Optical Characterizations. The optical images were collected by a custom microscope (Olympus BX53). The photoluminescence images were collected under the excitation of a light source (012-63000; X-CITE 120 REPL LAMP). The filter cube contains a bandpass filter (330-385 nm) for excitation and a dichroic mirror (cutoff wavelength, 400 nm) for light splitting and a filter (long pass 420 nm) for emission. The photoluminescence spectra were collected by a spectrometer (SpectraPro HRS-300). The timeresolved PL measurements were carried out using a 40x [numerical

- aperture (NA), 0.60] objective in a home-built microscope setup with a laser light generated by a picosecond-pulsed diode (LDH-P-C-450B, PicoQuant), pumping at 2.8 eV (full width at half-maximum, 50 ps).
- 4.5. Atomic Force Microscopy Images. Cypher ES Environmental AFM was used for the measurement with probe-type AC240TM-R3. During the imaging, the tapping mode was used.
- 4.6. XRD Measurements. XRD was measured using a powder Xray diffractometer (Panalytical Empyrean) with a Cu Klpha source. The wavelength ( $\lambda$ ) is 0.154 nm. The XRD measurements were performed on the as-grown MAPbI3 perovskites covering almost the entire surface of the SiO<sub>2</sub> (300 nm)/Si substrate. For thin samples, the 2D perovskite precursors were further exfoliated several times after being transferred onto silicon substrates. To do XRD measurements on thin and thick samples, the conversion reaction was conducted in 1 mL equilibrium solution for 1 h to ensure all the precursors are converted to MAPhI.
- 4.7. TEM Characterization for the Single-Layer MAPbl<sub>3</sub> Nanosheet and Twisted Structure. To acquire the high-resolution transmission electron microscopy (HRTEM) image, the ultrathin MAPbI<sub>3</sub> nanosheet was directly synthesized on polydimethylsiloxane (PDMS) substrate and then transferred onto SiN<sub>x</sub> TEM grid with the thickness of 5 nm. The 4D-STEM data sets were acquired using an event-driven Timepix3 direct electron camera equipped on probe aberration-corrected Thermo Fisher Advan-TEM. The accelerating voltage was 200 kV, and the convergence angle was set to 13 mrad. The collection angle of HAADF image was 48-200 mrad. The probe current was less than 0.2 pA, and the dwell time was 0.5  $\mu$ s. The 4D data sets were processed using the single sideband (SSB) method of 558 ptychography with a homemade python code. For the twisted MAPbI<sub>3</sub> structure, the MAPbI<sub>3</sub> nanosheet was transferred twice, and the twist angle was controlled by the optical transfer system.
- 4.8. Computational Details. DFT calculations were performed using the Vienna Ab initio Simulation Package (VASP), [refs S2-S4, Supporting Information] applying the projector augmented wave (PAW) pseudopotentials [ref S5, Supporting Information] and the generalized gradient approximation (GGA) of Perdew, Burke, and Ernzerhof (PBE) [ref S6, Supporting Information] for the exchangecorrelation energy. For all calculations, the kinetic energy cutoff for the plane-wave basis was set to 500 eV. The Brillouin zone was sampled based on a Monkhorst-Pack k-point mesh, with a reciprocal mesh of  $6 \times 6 \times 6$  for the MAPbI<sub>3</sub> cubic unit cell (with an optimized pseudocubic lattice constant of  $\sim$ 6.3 Å) and a 2 × 2 × 1 mesh for homojunction structures. For geometry optimization, the force convergence threshold was set to be −0.025 eV/Å and the selfconsistent energy convergence threshold is 10<sup>-6</sup> eV. DFT-D3 correction was applied along with GGA-PBE in all calculations to account for vdW interactions [ref S7, Supporting Information]. The electronic band structure was calculated at high-symmetry k-point paths, which is G (0,0,0), X (0.5,0,0), M (0.5,0.5,0), and R (0.5,0.5,0.5) for the cubic phase. Figures S10 and S11 show DFToptimized crystal structures and computed band structures for the cubic and tetragonal phases of MAPbI<sub>3</sub>. The MAPbI<sub>3</sub> homojunction structures were built from DFT-optimized layered MAPbI<sub>3</sub>. A 3 × 3 × 2 (001) MAPbI<sub>3</sub> slab was used to construct the bottom and top layers of the bilayer structure, and necessary horizontal displacements were performed to model the AB- and AA-stacking configurations. Electronic band edges were calculated based on a well-known average electrostatic potential alignment scheme involving bulk, surface slab, and interface calculations [refs S8 and S9, Supporting Information].

#### ASSOCIATED CONTENT

# **Solution** Supporting Information

The Supporting Information is available free of charge at https://pubs.acs.org/doi/10.1021/jacs.4c10298.

Images of solutions with different compositions, optical images of samples tracked with reaction time, more AFM images of the reaction tracked with different thickness, comparison of XRD results between thin and

thick samples, calculated results of bulk MAPbI3, and crystal parameters of 2D perovskites (PDF)

# AUTHOR INFORMATION

#### Corresponding Author

Letian Dou - Davidson School of Chemical Engineering, Department of Chemistry, and Birck Nanotechnology Center, Purdue University, West Lafayette, Indiana 47907, United States; orcid.org/0000-0001-6411-8591; Email: dou10@purdue.edu

#### Authors

- Shuchen Zhang Key Laboratory of Precision and Intelligent Chemistry, Department of Materials Science and Engineering, School of Chemistry and Materials Science, University of Science and Technology of China, Hefei 230026, China; Davidson School of Chemical Engineering, Purdue University, West Lafayette, Indiana 47907, United States
- Ke Ma Davidson School of Chemical Engineering, Purdue University, West Lafayette, Indiana 47907, United States; Global Institute of Future Technology, Shanghai Jiao Tong University, Shanghai 200240, China
- Biao Yuan Electron Microscopy for Materials Science, University of Antwerp, Antwerp 2020, Belgium; School of Physical Science and Technology, ShanghaiTech University, Shanghai 201210, China
- Jiaqi Yang School of Materials Engineering, Purdue University, West Lafayette, Indiana 47907, United States; orcid.org/0000-0001-7715-7864
- Yuan Lu School of Physical Science and Technology, Shanghai Tech University, Shanghai 201210, China
- Dewei Sun Department of Chemistry, Purdue University, West Lafayette, Indiana 47907, United States
- Jee Yung Park Davidson School of Chemical Engineering, Purdue University, West Lafayette, Indiana 47907, United States; o orcid.org/0000-0002-9814-6563
- **Zitang Wei** Davidson School of Chemical Engineering, Purdue University, West Lafayette, Indiana 47907, United
- Arun Mannodi-Kanakkithodi School of Materials Engineering, Purdue University, West Lafayette, Indiana 47907, United States; o orcid.org/0000-0003-0780-1583
- Yi Yu School of Physical Science and Technology, Shanghai Tech University, Shanghai 201210, China; orcid.org/0000-0003-4326-5992
- Libai Huang Department of Chemistry, Purdue University, West Lafayette, Indiana 47907, United States; o orcid.org/ 0000-0001-9975-3624
- **Timothy J. Pennycook** *Electron Microscopy for Materials* Science, University of Antwerp, Antwerp 2020, Belgium

Complete contact information is available at: https://pubs.acs.org/10.1021/jacs.4c10298

The authors declare no competing financial interest.

# ACKNOWLEDGMENTS

This work is primarily supported by the US Department of Energy, Office of Basic Energy Sciences under award number DE-SC0022082. The views expressed herein do not necessarily represent the views of the U.S. Department of Energy or the United States Government. L.D. acknowledges support from

National Science Foundation under award number 2143568-DMR. A.M.-K. acknowledges support from the School of Materials Engineering at Purdue University under account number F.10023800.05.002. S.Z. acknowledges support from Fundamental research funds for the central universities (KY2060000246). T. J. P. and B.Y. acknowledge funding from the European Research Council (ERC) under the European Union's Horizon 2020 Research and Innovation Programme via Grant Agreement No. 802123-HDEM. B. Y. acknowledges support from FWO Project, Belgium (G013122N).

# REFERENCES

- (1) Kim, M.; Jeong, J.; Lu, H.; Lee, T. K.; Eickemeyer, F. T.; Liu, Y.; Choi, I. W.; Choi, S. J.; Jo, Y.; Kim, H. B.; Mo, S. I.; Kim, Y. K.; Lee, H.; An, N. G.; Cho, S.; Tress, W. R.; Zakeeruddin, S. M.; Hagfeldt, A.; Kim, J. Y.; Grätzel, M.; Kim, D. S. Conformal quantum dot-SnO<sub>2</sub> layers as electron transporters for efficient perovskite solar cells. Science 2022, 375 (6578), 302-306.
- (2) Ni, Z.; Bao, C.; Liu, Y.; Jiang, Q.; Wu, W.; Chen, S.; Dai, X.; Chen, B.; Hartweg, B.; Yu, Z.; Holman, Z.; Huang, J. Resolving spatial and energetic distributions of trap states in metal halide perovskite solar cells. Science 2020, 367 (6484), 1352-1358.
- (3) Luo, D.; Su, R.; Zhang, W.; Gong, Q.; Zhu, R. Minimizing nonradiative recombination losses in perovskite solar cells. Nat. Rev. *Mater.* **2020**, 5 (1), 44–60.
- (4) Ma, K.; Atapattu, H. R.; Zhao, Q.; Gao, Y.; Finkenauer, B. P.; Wang, K.; Chen, K.; Park, S. M.; Coffey, A. H.; Zhu, C.; Huang, L.; Graham, K. R.; Mei, J.; Dou, L. Multifunctional conjugated ligand engineering for stable and efficient perovskite solar cells. Adv. Mater. **2021**, 33 (32), No. 2100791.
- (5) Fu, Y.; Zhu, H.; Chen, J.; Hautzinger, M. P.; Zhu, X.-Y.; Jin, S. Metal halide perovskite nanostructures for optoelectronic applications and the study of physical properties. Nat. Rev. Mater. 2019, 4 (3),
- (6) Deng, S.; Shi, E.; Yuan, L.; Jin, L.; Dou, L.; Huang, L. Longrange exciton transport and slow annihilation in two-dimensional hybrid perovskites. Nat. Commun. 2020, 11 (1), 1-8.
- (7) Herz, L. M. Charge-carrier mobilities in metal halide perovskites: fundamental mechanisms and limits. ACS Energy Lett. 2017, 2 (7), 1539 - 1548
- (8) Filip, M. R.; Eperon, G. E.; Snaith, H. J.; Giustino, F. Steric engineering of metal-halide perovskites with tunable optical band gaps. Nat. Commun. 2014, 5 (1), 1-9.
- (9) Shi, E.; Gao, Y.; Finkenauer, B. P.; Akriti; Coffey, A. H.; Dou, L. Two-dimensional halide perovskite nanomaterials and heterostructures. Chem. Soc. Rev. 2018, 47 (16), 6046-6072.
- (10) Ricciardulli, A. G.; Yang, S.; Smet, J. H.; Saliba, M. Emerging perovskite monolayers. Nat. Mater. 2021, 20 (10), 1325-1336.
- (11) Blancon, J. C.; Tsai, H.; Nie, W.; Stoumpos, C. C.; Pedesseau, L.; Katan, C.; Kepenekian, M.; SOE, C. M. M.; Appavoo, K.; Sfeir, M. Y.; Tretiak, S.; Ajayan, P. M.; Kanatzidis, M. G.; Even, J.; Crochet, J. J.; Mohite, A. D. Extremely efficient internal exciton dissociation through edge states in layered 2D perovskites. Science 2017, 355 (6331), 1288-1292.
- (12) Yang, Y.; Yang, M.; Li, Z.; Crisp, R.; Zhu, K.; Beard, M. C. Comparison of recombination dynamics in CH3NH3PbBr3 and CH<sub>3</sub>NH<sub>3</sub>PbI<sub>3</sub> perovskite films: influence of exciton binding energy. J. Phys. Chem. Lett. 2015, 6 (23), 4688-4692.
- (13) Dyksik, M.; Duim, H.; Maude, D. K.; Baranowski, M.; Loi, M. A.; Plochocka, P. Brightening of dark excitons in 2D perovskites. Sci. Adv. 2021, 7 (46), No. eabk0904.
- (14) Liu, Y.; Dong, Y.; Zhu, T.; Ma, D.; Proppe, A.; Chen, B.; Zheng, C.; Hou, Y.; Lee, S.; Sun, B.; Jung, E. H.; Yuan, F.; Wang, Y.; Sagar, L. K.; Hoogland, S.; García de Arquer, F. P.; Choi, M.; Singh, K.; Kelley, S. O.; Voznyy, O.; Lu, Z.; Sargent, E. H. Bright and stable light-emitting diodes based on perovskite quantum dots in perovskite matrix. J. Am. Chem. Soc. 2021, 143 (38), 15606-15615.

- (15) Kim, Y.; Yassitepe, E.; Voznyy, O.; Comin, R.; Walters, G.; Gong, X.; Kanjanaboos, P.; Nogueira, A. F.; Sargent, E. H. Efficient luminescence from perovskite quantum dot solids. *ACS Appl. Mater. Interfaces* **2015**, *7* (45), 25007–25013.
- (16) Yan, R.; Gargas, D.; Yang, P. Nanowire photonics. *Nat. Photonics* **2009**, 3 (10), 569–576.
- (17) Xia, Y.; Yang, P.; Sun, Y.; Wu, Y.; Mayers, B.; Gates, B.; Yin, Y.; Kim, F.; Yan, H. One-dimensional nanostructures: synthesis, characterization, and applications. *Adv. Mater.* **2003**, *15* (5), 353–389.
- (18) Saparov, B.; Mitzi, D. B. Organic-inorganic perovskites: structural versatility for functional materials design. *Chem. Rev.* **2016**, 116 (7), 4558–4596.
- (19) Weidman, M. C.; Goodman, A. J.; Tisdale, W. A. Colloidal halide perovskite nanoplatelets: an exciting new class of semi-conductor nanomaterials. *Chem. Mater.* **2017**, *29* (12), 5019–5030.
- (20) Pacchioni, G. Highly efficient perovskite LEDs. Nat. Rev. Mater. 2021, 6 (2), 108–108.
- (21) Rainò, G.; Becker, M. A.; Bodnarchuk, M. I.; Mahrt, R. F.; Kovalenko, M. V.; Stöferle, T. Superfluorescence from lead halide perovskite quantum dot superlattices. *Nature* **2018**, *563* (7733), *671*–675.
- (22) Spanopoulos, I.; Hadar, I.; Ke, W.; Tu, Q.; Chen, M.; Tsai, H.; He, Y.; Shekhawat, G.; Dravid, V. P.; Wasielewski, M. R.; Mohite, A. D.; Stoumpos, C. C.; Kanatzidis, M. G. Uniaxial expansion of the 2D Ruddlesden—Popper perovskite family for improved environmental stability. *J. Am. Chem. Soc.* **2019**, *141* (13), 5518—5534.
- (23) Gao, Y.; Shi, E.; Deng, S.; Shiring, S. B.; Snaider, J. M.; Liang, C.; Yuan, B.; Song, R.; Janke, S. M.; Liebman-Peláez, A.; Yoo, P.; Zeller, M.; Boudouris, B. W.; Liao, P.; Zhu, C.; Blum, V.; Yu, Y.; Savoie, B. M.; Huang, L.; Dou, L. Molecular engineering of organic—inorganic hybrid perovskites quantum wells. *Nat. Chem.* **2019**, *11* (12), 1151–1157.
- (24) Leng, K.; Abdelwahab, I.; Verzhbitskiy, I.; Telychko, M.; Chu, L.; Fu, W.; Chi, X.; Guo, N.; Chen, Z.; Chen, Z.; Zhang, C.; Xu, Q.; Lu, J.; Chhowalla, M.; Eda, G.; Loh, K. P. Molecularly thin two-dimensional hybrid perovskites with tunable optoelectronic properties due to reversible surface relaxation. *Nat. Mater.* **2018**, *17* (10), 908–914.
- (25) Su, R.; Fieramosca, A.; Zhang, Q.; Nguyen, H. S.; Deleporte, E.; Chen, Z.; Sanvitto, D.; Liew, T. C. H.; Xiong, Q. Perovskite semiconductors for room-temperature exciton-polaritonics. *Nat. Mater.* **2021**, *20* (10), 1315–1324.
- (26) Blancon, J. C.; Even, J.; Stoumpos, C. C.; Kanatzidis, G.; Mohite, A. D. Semiconductor physics of organic—inorganic 2D halide perovskites. *Nat. Nanotechnol.* **2020**, *15* (12), 969–985.
- (27) Li, P.; Chen, Y.; Yang, T.; Wang, Z.; Lin, H.; Xu, Y.; Li, L.; Mu, H.; Shivananju, B. N.; Zhang, Y.; Zhang, Q.; Pan, A.; Li, S.; Tang, D.; Jia, B.; Zhang, H.; Bao, Q. Two-dimensional CH<sub>3</sub>NH<sub>3</sub>PbI<sub>3</sub> perovskite nanosheets for ultrafast pulsed fiber lasers. *ACS Appl. Mater. Interfaces* **2017**, *9*, 12759–12765.
- (28) Wang, Z.; Ou, Q.; Zhang, Y.; Zhang, Q.; Hoh, H. Y.; Bao, Q. Degradation of two-dimensional CH<sub>3</sub>NH<sub>3</sub>PbI<sub>3</sub> perovskite and CH<sub>3</sub>NH<sub>3</sub>PbI<sub>3</sub>/graphene heterostructure. *ACS Appl. Mater. Interfaces* **2018**, *10*, 24258–24265.
- (29) Sun, Y.; Yin, Y.; Pols, M.; Zhong, J.; Huang, Z.; Liu, B.; Liu, J.; Wang, W.; Xie, H.; Zhan, G.; Zhou, Z.; Zhang, W.; Wang, P.; Zha, C.; Jiang, X.; Ruan, Y.; Zhu, C.; Brocks, G.; Wang, X.; Wang, L.; Wang, J.; Tao, S.; Huang, W. Engineering the phases and heterostructures of ultrathin hybrid perovskite nanosheets. *Adv. Mater.* **2020**, 32, No. 2002392.
- (30) Adjokatse, S.; Fang, H.-H.; Duim, H.; Loi, M. A. Scalable fabrication of high-quality crystalline and stable FAPbI<sub>3</sub> thin films by combining doctor-blade coating and the cation exchange reaction. *Nanoscale* **2019**, *11*, 5989–5997.
- (31) Zhang, S.; Jin, L.; Lu, Y.; Zhang, L.; Yang, J.; Zhao, Q.; Sun, D.; Thompson, J. J. P.; Yuan, B.; Ma, K.; Akriti; Park, J. P.; Lee, Y. H.; Wei, Z.; Finkenauer, B. P.; Blach, D. D.; Kumar, S.; Peng, H.; Mannodi-Kanakkithodi, A.; Yu, Y.; Malic, E.; Lu, G.; Dou, L.; Huang,

- L. Moiré Superlattices in Twisted Two-Dimensional Halide Perovskites. *Nat. Mater.* **2024**, 23, 1222.
- (32) Zhao, Y.; Zhu, K. Three-step sequential solution deposition of PbI<sub>2</sub>-free CH<sub>3</sub>NH<sub>3</sub> PbI<sub>3</sub> perovskite. *J. Mater. Chem. A* **2015**, 3 (17), 9086–9091.
- (33) Zhang, T.; Yang, M.; Zhao, Y.; Zhu, K. Controllable sequential deposition of planar CH<sub>3</sub>NH<sub>3</sub>PbI<sub>3</sub> perovskite films via adjustable volume expansion. *Nano Lett.* **2015**, *15* (6), 3959–3963.
- (34) Pan, D.; Fu, Y.; Spitha, N.; Zhao, Y.; Roy, C. R.; Morrow, D. J.; Kohler, D. D.; Wright, J. C.; Jin, S. Deterministic fabrication of arbitrary vertical heterostructures of two-dimensional Ruddlesden—Popper halide perovskites. *Nat. Nanotechnol.* **2021**, *16* (2), 159–165.
- (35) Liu, J.; Xue, Y.; Wang, Z.; Xu, Z.; Zheng, C.; Weber, B.; Song, J.; Wang, Y.; Lu, Y.; Zhang, Y.; Bao, Q. Two-dimensional CH<sub>3</sub>NH<sub>3</sub>PbI<sub>3</sub> perovskite: synthesis and optoelectronic application. *ACS Nano* **2016**, *10* (3), 3536–3542.
- (36) Li, D.; Wang, K.; Tang, J.; Zhao, Y.; Elhaes, H.; Tahir, M.; Ibrahim, M. A.; Li, Y. Efficient photosensitized singlet oxygen generation in two-dimensional perovskite nanosheets via energy transfer. *Appl. Surf. Sci.* **2023**, *613*, No. 155991.
- (37) Deng, Y. H.; Nest, L. G. Analysis of misidentifications in TEM characterisation of organic-inorganic hybrid perovskite material. *J. Microsc.* **2021**, 282, 195–204.
- (38) Pennycook, T. J.; Martinez, G. T.; Nellist, P. D.; Meyer, J. C. High dose efficiency atomic resolution imaging via electron ptychography. *Ultramicroscopy* **2019**, *196*, 131–135.
- (39) Li, H.; Li, S.; Regan, E. C.; Wang, D.; Zhao, W.; Kahn, S.; Yumigeta, K.; Blei, M.; Taniguchi, T.; Watanabe, K.; Tongay, S.; Zettl, A.; Crommie, M. F.; Wang, F. Imaging two-dimensional generalized Wigner crystals. *Nature* **2021**, *597*, 650–654.
- (40) Yuan, L.; Zheng, B.; Kunstmann, J.; Brumme, T.; Kuc, A. B.; Ma, C.; Deng, S.; Blach, D.; Pan, A.; Huang, L. Twist-angle-dependent interlayer exciton diffusion in WS<sub>2</sub>–WSe<sub>2</sub> heterobilayers. *Nat. Mater.* **2020**, *19* (6), 617–623.
- (41) Liu, L.; Sun, Y.; Cui, X.; Qi, K.; He, X.; Bao, Q.; Ma, W.; Lu, J.; Fang, H.; Zhang, P.; Zheng, L.; Yu, L.; Singh, D. J.; Xiong, Q.; Zhang, L.; Zheng, W. Bottom-up growth of homogeneous Moiré superlattices in bismuth oxychloride spiral nanosheets. *Nat. Commun.* **2019**, *10*, 1–10
- (42) Zhang, L.; Zhang, X.; Lu, G. Predictions of moiré excitons in twisted two-dimensional organic—inorganic halide perovskites. *Chem. Sci.* **2021**, *12*, 6073—6080.